Direct measurement of non-thermal electron acceleration from magnetically driven reconnection in a laboratory plasma

Abraham Chien, Lan Gao, Shu Zhang, Hantao Ji, Eric Blackman, William Daughton, Adam Stanier, Ari Le, Fan Guo, Russ Follett, et al.

Direct measurement of non-thermal electron acceleration from magnetically driven reconnection in a laboratory plasma

Abraham Chien,[1, a)] Lan Gao,[2] Shu Zhang,[1] Hantao Ji,[1, 2, b)] Eric G. Blackman,[3] William Daughton,[4] Adam Stanier,[4] Ari Le,[4] Fan Guo,[4] Russ Follett,[5] Hui Chen,[6] Gennady Fiksel,[7] Gabriel Bleotu,[8] Robert C. Cauble,[6] Sophia Chen,[8] Alice Fazzini,[9] Kirk Flippo,[4] Omar French,[10] Dustin Froula,[5] Julien Fuchs,[9] Shinsuke Fujioka,[11] Kenneth Hill,[2] Sallee Klein,[7] Carolyn Kuranz,[7] Philip Nilson,[5] Alexander Rasmus,[4] and Ryunosuke Takizawa[11]

[1)]*Department of Astrophysical Sciences, Princeton University, Princeton, New Jersey 08544 USA*
[2)]*Princeton Plasma Physics Laboratory, Princeton University, Princeton, New Jersey 08543 USA*
[3)]*Department of Physics and Astronomy, University of Rochester, Rochester, New York 14627 USA*
[4)]*Los Alamos National Laboratory, Los Alamos, New Mexico 87545 USA*
[5)]*Laboratory for Laser Energetics, University of Rochester, Rochester, New York 14623 USA*
[6)]*Lawrence Livermore National Laboratory, Livermore, California 94550 USA*
[7)]*University of Michigan, Ann Arbor, Michigan 48109 USA*
[8)]*ELI-NP, "Horia Hulubei" National Institute for Physics and Nuclear Engineering, 30 Reactorului Street, RO-077125, Bucharest-Magurele, Romania*
[9)]*LULI-CNRS, CEA, UPMC Univ Paris 06: Sorbonne Universite, Ecole Polytechnique, Institut Polytechnique de Paris, F-91128 Palaiseau Cedex, France*
[10)]*University of Maryland, Baltimore County, Baltimore, Maryland 21250 USA*
[11)]*Institute of Laser Engineering, Osaka University, Osaka, 565-0871, Japan*

(Dated: 3 June 2021)

Magnetic reconnection is a ubiquitous astrophysical process that rapidly converts magnetic energy into some combination of plasma flow energy, thermal energy, and non-thermal energetic particles, particularly, and energetic electrons[1,2]. Various reconnection acceleration mechanisms[3] in different low-β (plasma-to-magnetic pressure ratio) and collisionless environments[4–9] have been proposed theoretically and studied numerically[10–15], including first- and second-order Fermi acceleration[16], betatron acceleration[17], parallel electric field acceleration along magnetic fields[18], and direct acceleration by the reconnection electric field[19]. However, none of them have been heretofore confirmed experimentally, as the direct observation of non-thermal particle acceleration in laboratory experiments has been difficult due to short Debye lengths for *in-situ* measurements and short mean free paths for *ex-situ* measurements. Here we report the direct measurement of accelerated non-thermal electrons from low-β magnetically driven reconnection in experiments using a laser-powered capacitor coil platform. We use kiloJoule lasers to drive parallel currents to reconnect MegaGauss-level magnetic fields in a quasi-axisymmetric geometry[20–22]. The angular dependence of the measured electron energy spectrum and the resulting accelerated energies, supported by particle-in-cell simulations, indicate that the mechanism of direct electric field acceleration by the out-of-plane reconnection electric field is at work. Scaled energies using this mechanism show direct relevance to astrophysical observations. Our results therefore validate one of the proposed acceleration mechanisms by reconnection, and establish a new approach to study reconnection particle acceleration with laboratory experiments in relevant regimes.

Magnetic reconnection, the process by which magnetic field topology in a plasma is reconfigured, rapidly converts magnetic energy into some combination of bulk flow, thermal, and accelerated particles. The latter is a prominent feature of presumed reconnection regions in nature, and as such, reconnection can be thought of as an efficient particle accelerator in low-β ($\lesssim 1$), collisionless plasmas where abundant magnetic free energy per particle is available. Electron acceleration up to ~ 300 keV, for example, has been observed in Earth's magnetotail[5] and the measured spectra in X-ray, extreme ultraviolet, and microwave wavelengths from solar flares include a non-thermal power law component, indicating a large suprathermal electron population[4,6,9]. Reconnection has been suggested as the underlying source of these non-thermal electrons. Gamma-ray flares from the Crab Nebula are another example, exhibiting particle acceleration up to 10^{15} eV, which cannot be explained by shock acceleration mechanisms[7,8,23].

The efficient acceleration of charged particles by magnetic reconnection has been studied theoretically and numerically[11–13,24–26], and various acceleration mechanisms, such as parallel electric field acceleration and Fermi acceleration, have been proposed[16–19]. However, thus far, no direct measurements of non-thermal particle acceleration due to reconnection have been made in laboratory experiments to confirm or contradict these mechanisms. Short Debye lengths and mean free paths have limited most *in-situ* and *ex-situ* detection of the predicted energetic electrons, respectively, while indirect measurements of energetic electrons are necessarily limited by specific models assumed for radiation and acceleration mechanisms[27–29].

[a)]Electronic mail: achien2@pppl.gov
[b)]Electronic mail: hji@pppl.gov

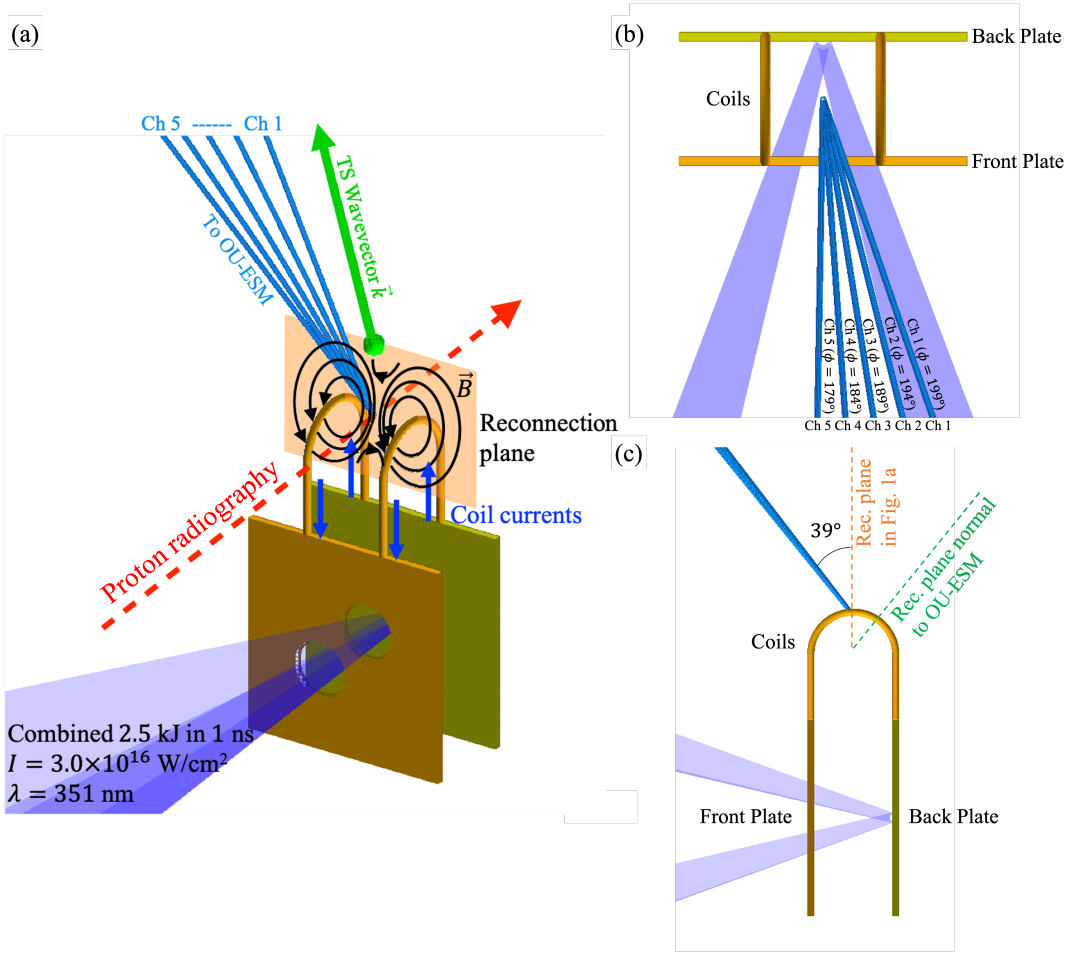

FIG. 1: **Experimental setup of low-β, magnetically driven reconnection using laser-powered capacitor coils. a,** The capacitor-coil target is driven by two long-pulse lasers, passing through the front holes and irradiating the back plate. An electrostatic potential is created between the (capacitor) plates, and large currents (blue) are generated in the parallel U-shaped coils. The resulting magnetic fields form a reconnection structure between the coils. Major diagnostics are target-normal sheath acceleration (TNSA) proton radiography and the Osaka University – Electron Spectrometer. The OU-ESM is positioned 37.5 cm away from the main interaction, at an angle 39° from the vertical. 5 independent channels are situated with 5° between each channel, allowing a measurement of the angular spread of electrons in the azimuthal direction. Thomson scattering measurements were taken in a similar experiment to diagnose plasma parameters: the green ball shows the probing volume, and the Thomson scattering wavevector $\vec{k}$ is also shown. **b,** A top-down view of the main target is shown, along with the OU-ESM channel orientation in the azimuthal direction. **c,** A side-on view of the main target shows the relative polar orientation of the OU-ESM channels. The orange vertical dashed line represents the reconnection plane shown in **a**, and the green dashed line represents the reconnection plane that is normal to the OU-ESM line of sight.

High-energy-density (HED) plasmas[20–22,30–34] have recently emerged as novel platforms to study magnetic reconnection. In particular, direct measurements of charged particle spectra are possible due to a large electron mean free path relative to the detector distance. Importantly, low-β, collisionless, magnetically driven reconnection is achievable using laser-powered capacitor coils[20–22], allowing relevant conditions to astrophysical environments. Here, using this experimental reconnection platform, we directly detect non-thermal electron acceleration from reconnection, and combined with particle-in-cell simulations, infer a primary acceleration mechanism of direct electric field acceleration by the reconnection electric field.

Our experiments using laser-powered capacitor coils were performed at the OMEGA EP facility at the Laboratory for Laser Energetics (LLE). The experimental setup, with diagnostic locations, is shown in Fig. 1. The capacitor-coil target is driven with two laser pulses, each delivering 1.25-kiloJoule of laser energy in a 1-ns square temporal profile at a wavelength of 351 nm. The corresponding on-target laser intensity is $\sim 3\times10^{16}$ W/cm^2. Due to the laser interaction, strong currents are driven in the coils. In targets with two parallel coils, a magnetic reconnection field geometry is created between the coils, and in targets with one coil, a simple magnetic field around a wire is produced, representing a non-reconnection control case. Further information on capacitor coil target op-

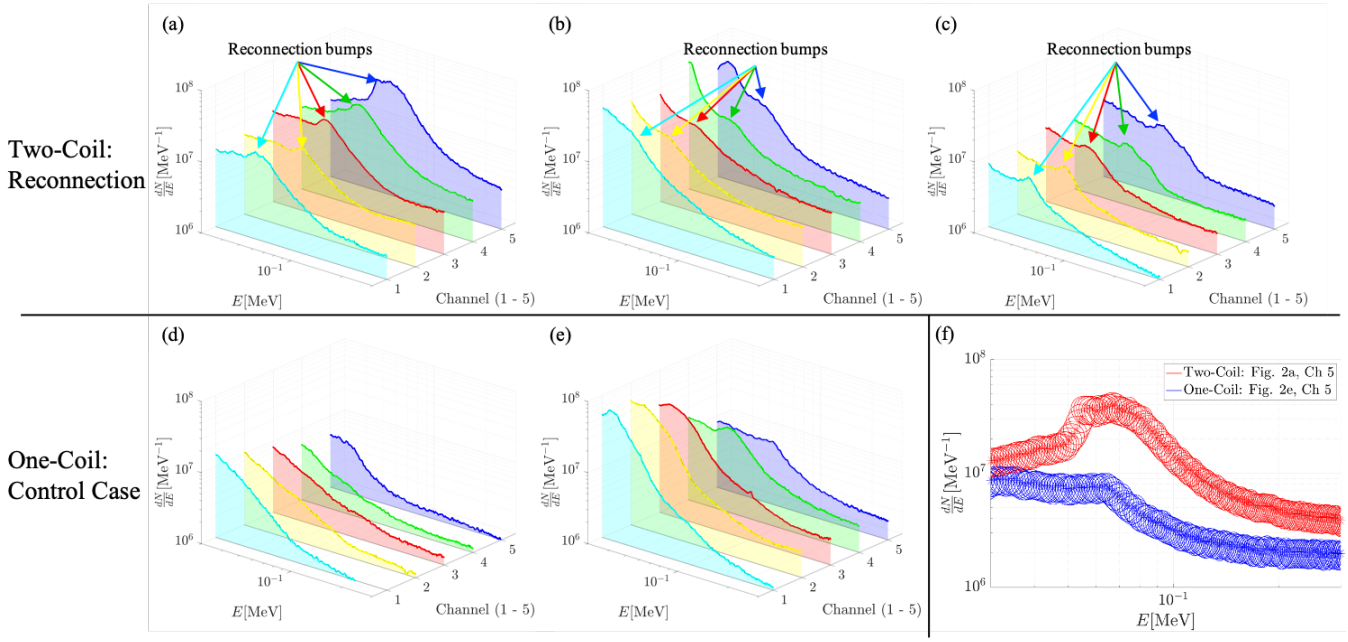

FIG. 2: **Experimental particle spectra exhibit conspicuous evidence for non-thermal acceleration bumps in reconnection cases, that are absent in non-reconnection cases.** Particle spectra from the OU-ESM are presented for 5 experimental shots: 3 two-coil reconnection cases (**a, b, c**) and 2 one-coil control cases (**d, e**). 5 colors represent the 5 channels spread in azimuthal angle (Fig. 1b). Despite shot-to-shot variations in signal level, in the reconnection cases, spectral bumps are observed in the 40–70 keV range. These bumps are strongest in Channel 5, representing a near-face-on view of the target, and decrease with larger azimuthal angle, with the weakest bumps in Channel 1, representing 19° off normal. Such a trend is noticeably absent in the control cases, where overall weaker signal levels are observed. A feature appearing to be a spectral bump is observed in **e**, but it is, in fact, a deficiency in the low-energy range: due to the coil position on the left, low-energy electrons are preferentially accelerated toward large $\theta - z$ pitch angle, resulting in an absence in Channels 4 and 5. **f,** A plot of **a** (reconnection) and **e** (control) shots, Channel 5 are shown with ellipses representing the vertical and horizontal error bars at each point. In the reconnection case, the bump clearly exceeds error bars, but in the control case, there is no spectral bump beyond the error bars, further supporting the low-energy deficiency described in **e**.

eration and design are provided in the Methods section.

The coil current profile can be approximated by a linear rise during the laser pulse ($0 < t < t_{\text{rise}}$), followed by an exponential decay after laser turn-off. Target sheath normal acceleration (TNSA)[35] proton radiography measurements indicated a maximum coil current at $t_{\text{rise}} = 1$ ns of 57 kA, corresponding to a magnetic field at the center of the coils of 110 T, with a subsequent exponential decay time of $t_{\text{decay}} = 8.6$ ns[21]. During the current rise, the magnetic field strengthens, driving "push"-phase reconnection, where field lines are pushed into the reconnection region, and during current decay, "pull" reconnection occurs, where field lines are pulled out of the reconnection region[36]. Due to the short timescale of the push phase relative to the pull phase, reconnection is driven more strongly during the push phase and dominates the duration of particle acceleration.

We used Thomson scattering to diagnose the reconnecting copper plasma in a similar experiment on the OMEGA laser, and found electron density $n_e \simeq 3 \times 10^{18}$ cm^{-3}, ion density $n_i \simeq 1.7 \times 10^{17}$ cm^{-3}, electron and ion temperatures $T_e \simeq T_i \simeq$ 400 eV. Due to the large $Z = 18$, the ion plasma pressure is negligible compared to the electron plasma pressure, and the ratio of plasma pressure to magnetic pressure $\beta \simeq 0.05$. The experiments are therefore firmly in the low-β regime, most pertinent for particle acceleration in astrophysical conditions. The Lundquist number is $10^3 - 10^4$, representing collisionless reconnection. The reconnection system size is defined by the inter-coil distance of $L = 600$ μm, and when normalized by the ion skin depth d_i, the normalized system size $L/d_i \simeq 1.4$. Due to the small system size, the reconnection is deeply in the electron-only regime[37], where ions are decoupled.

A time-integrated electron spectrometer – the Osaka University Electron Spectrometer (OU-ESM) – was used to measure the electron energy spectra. It is located 37.5 cm away from the coils, at a polar angle of 39° and scans an azimuthal range of 179° – 199° with five equally-spaced detection channels. The OU-ESM channel orientation is shown in Fig. 1(b,c). Further details regarding the OU-ESM are given in the Methods section. Particle spectrometer data are collected for a total of five shots, with three double-coil reconnection shots, and two single-coil control shots. The OU-ESM data for the five shots are shown in Fig. 2.

Small differences in the laser energy profile and target properties between shots causes variations in otherwise nominally identical cases as seen in Fig. 2. However, focusing on the angular dependence across the channels for each shot reveals a key feature in the electron spectra: non-thermal "bumps" in the reconnection cases that do not appear in the control cases.

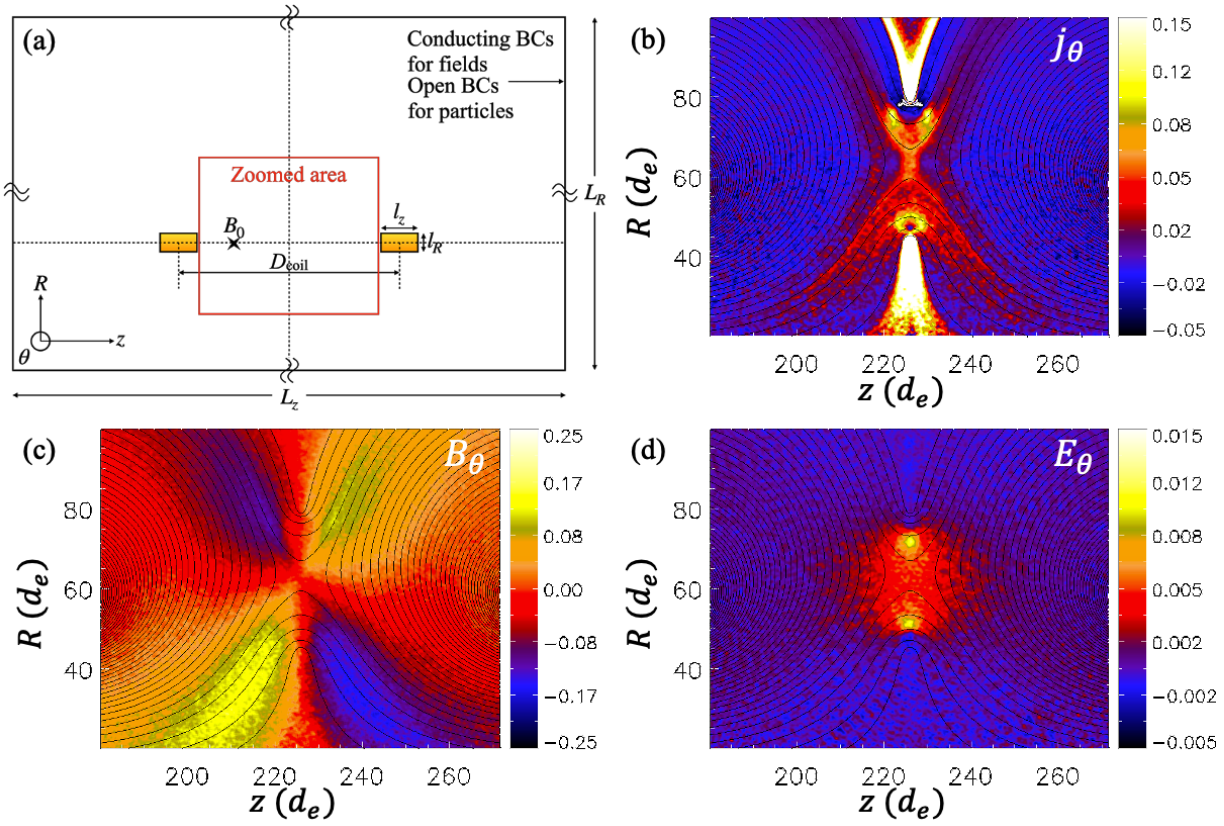

FIG. 3: **Particle-in-cell simulation setup of capacitor-coil reconnection demonstrates push reconnection and quadrupole out-of-plane magnetic fields. a,** Schematic of the 2-D cylindrical simulation box used in VPIC modeling, with z the axis of symmetry and R the radial direction. The azimuthal angle θ is directed out-of-the-page. Two rectangular coils are situated at $R = R_{coil}$ with center-to-center separation of D_{coil}. The reference magnetic field B_0 is measured upstream from the coils. Conducting boundary conditions for fields and open boundary conditions for particles are stipulated. Current is injected in the coils with time, replicating the experimental current profile. Time evolution of fields are evaluated relative to the current rise time $t_{\rm rise}$, to keep the magnetic field drive consistent. All measurements are taken in the "zoomed" box area, marked in red. The outer box boundary is not to scale.**b-d** Profiles of out-of-plane electric current density j_θ, out-of-plane magnetic field B_θ, and reconnection electric field E_θ in the red rectangular zoomed area are shown at $t = 1.55\ t_{rise}$, overlaid with magnetic field lines. B_θ shows a characteristic quadrupole field structure from decoupled electron and ion flows. A noticeable reconnection electric field is observed around the current sheet near the magnetic null, with the orientation indicating push reconnection. j_θ, B_θ, and E_θ are shown in the respective normalized units: $j_0 = en_{e0}c$, $B_0 = m_e\omega_{pe}/e$, and $E_0 = cB_0 = m_e\omega_{pe}c/e$.

The bumps span the $50-70$ keV range, and they are most pronounced at the near-normal Channel 5 ($\phi = 179^\circ$) and weaken with increasing angle from normal. In contrast, the one-coil control cases do not exhibit consistent spectral bumps, and generally exhibit lower signal level. One exception is Figure 2e, which represents a one-coil shot with the coil on the left side (as viewed from the front of the target). Due to the coil magnetic field, low-energy electrons are deflected toward higher ϕ, resulting in an electron deficiency in Channel 5 and to a lesser extent, Channel 4.

These spectral bumps demonstrate non-thermal electron acceleration, and the detection angle dependence of the bump sizes suggests a directional anisotropy in the accelerated electron population. The strongest non-thermal population is seen in the direction out of the reconnection plane, anti-parallel to the reconnection electric field, indicating its responsibility for the direct acceleration.

Interpretation of this particle acceleration mechanisms is supported by particle-in-cell simulations. We conducted 2-D cylindrical particle-in-cell (PIC) simulations using the VPIC code[38] in order to model kinetic effects and simulated particle energy spectra (Fig. 3a shows the geometric setup). The z-direction is the axis of symmetry, R is the radial direction, and θ is the out-of-plane direction. Two rectangular-cross-section coils are placed in the simulation box, representing cross-sectional slices of the experimental U-shaped coils. Reconnection is driven by prescribing and injecting currents within the coils. We prioritize realistic mass ratio and β in the simulation, at the expense of the reduced but scaled electron plasma frequency to electron gyrofrequency ratio, ω_{pe}/Ω_{ce}, due to the limited computational resources. Further details for the simulation setup are described in the Methods section.

The PIC simulation results demonstrate strong reconnection driven by the coil magnetic fields, with a typical out-of-

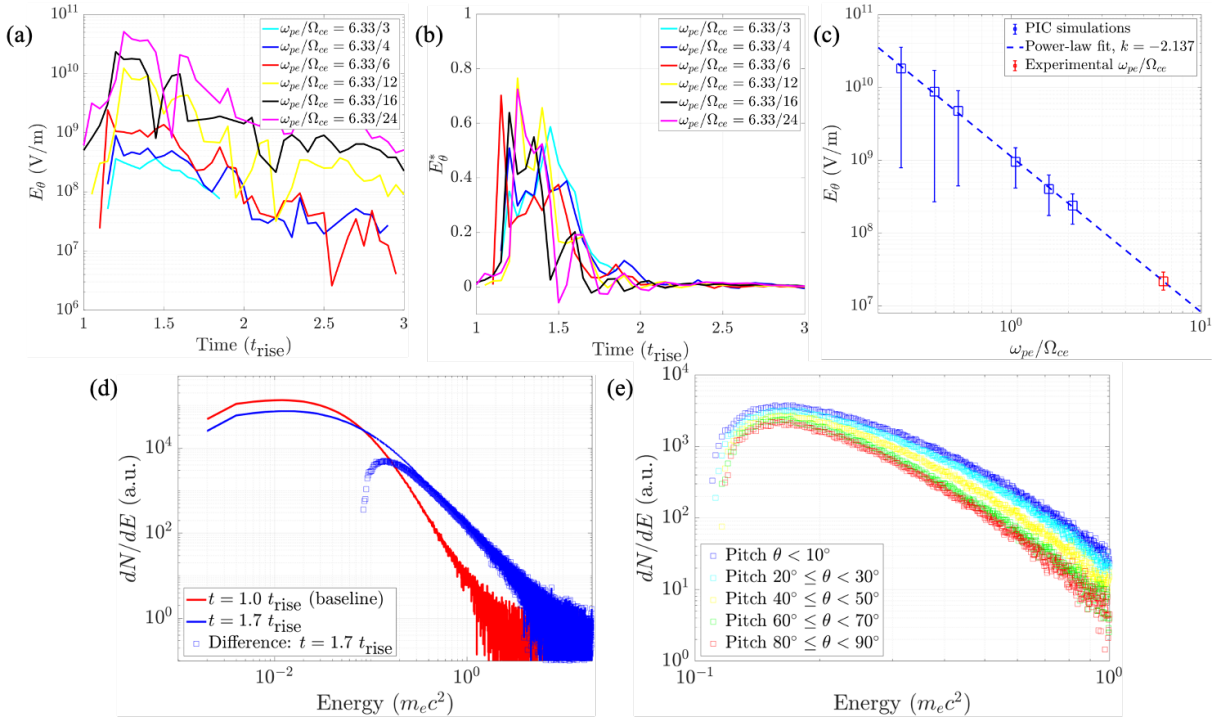

FIG. 4: **Particle-in-cell simulations of capacitor-coil reconnection validates electron acceleration by the reconnection electric field. a,** The reconnection electric field time-evolution are shown for varying ω_{pe}/Ω_{ce}. From the period of $t \sim (1-3)t_{rise}$, the reconnection electric field is prominent. **b,** The reconnection rate, E^*_θ, is obtained by normalizing the reconnection electric field by the upstream $V_A \times B_0$, where V_A is the Alfvén speed computed with the upstream magnetic field B_0 and ion mass density in the reconnection region. E^*_θ is generally constant across the ω_{pe}/Ω_{ce} scan. The non-normalized reconnection electric field strength decreases with increasing ω_{pe}/Ω_{ce}. **c,** A power law is fit to the reconnection electric field strength dependence on ω_{pe}/Ω_{ce}. Extrapolating to the experimental parameters value of $\omega_{pe}/\Omega_{ce} = 6.33$ gives $E_\theta = 2.18\ (1.64, 2.92) \times 10^7\ V/m$ (Parenthesized values represent 95% confidence interval). **d,** The electron particle spectrum is measured within the zoomed box and with limiting the $\theta - z$ pitch angle to 10°. The particle spectrum for $\omega_{pe}/\Omega_{ce} = 6.33/4$ is shown: $t \sim 1.0 t_{rise}$ (red) represents a baseline spectrum. The maximum non-thermal tail is seen at $t \sim 1.7 t_{rise}$, consistent with the reconnection electric field time dependence. The non-thermal difference from the baseline spectrum is shown in blue squares. **e,** Non-thermal difference spectra are shown for $t = 1.7 t_{rise}$, separated by $\theta - z$ pitch angle. Small pitch angles (near normal to the reconnection plane) correspond to higher-energy tails, while large pitch angles (near parallel to the reconnection plane) show smaller non-thermal acceleration.

plane quadrupole structure (Fig. 3c), indicative of scale separation between ions and electrons[39,40]. In addition, a clear out-of-plane reconnection electric field is observed around the X-point, and the orientation of the electric field is consistent with push reconnection (see Fig. 3d).

To obtain the reconnection rate, the reconnection electric field is typically normalized by an upstream $V_A \times B_0$, where B_0 is the upstream magnetic field strength and $V_A = B_0/\sqrt{\mu_0 m_i n_i}$ is the Alfvén velocity calculated with the ion density at the X-point. Figure 4b shows that the strongest reconnection occurs from $t \sim t_{rise} - 1.7 t_{rise}$, for all simulated values of ω_{pe}/Ω_{ce}. The diffusion time of the magnetic field through the plasma explains why this timing does not correspond to the expected period of push reconnection at $t < t_{rise}$. In nearly all cases, the reconnection rate reaches maximum values of $0.6 - 0.7$, significantly higher than the typical ~ 0.1 rate expected for collisionless electron-ion reconnection[41]: this is typical of electron-only reconnection, which is characterized by a normalized system size[42] $L/d_i \lesssim 5$.

The magnitude of the reconnection electric field varies with ω_{pe}/Ω_{ce}, since the magnetic field strength scales inversely with ω_{pe}/Ω_{ce}. To predict the scaling, we approximate $E_\theta \propto V_A \times B \propto B^2 \propto (\omega_{pe}/\Omega_{ce})^{-2}$, implying an inverse quadratic relationship. Plotting the simulated reconnection electric field strength for various ω_{pe}/Ω_{ce} demonstrates an inverse dependence (Fig. 4a), consistent with a power law index of $k = -2.137$ (Fig. 4c). Extrapolating the reconnection electric field strength to experimental parameters gives $E_\theta = 2.18\ (1.64, 2.92) \times 10^7\ V/m$, with parenthesized values representing the 95% confidence interval.

Finally, the PIC simulations demonstrate non-thermal particle acceleration during the push phase of reconnection. Various filters are applied to the electron population to select the electrons that best compare to the experimental spectra. First, to focus on the electrons that are affected by reconnection, electrons are measured only within the zoomed-in simulation area shown in Fig. 3a, Second, the $\theta - z$ pitch angle is limited to select electrons that can escape and be measured by the OU-ESM detector. For our 2-D axisymmetric simulation, we do not limit the $\theta - R$ pitch angle, since for any fixed detec-

TABLE I: Comparisons of maximum electron energy between measured values from low-β reconnection sources, as a partial list from Ji & Daughton (2011)[43], and their estimation based on reconnection electric field acceleration, $0.1V_ABd$. Here d is a characteristic acceleration distance which is taken to the system size for maximum energy. Unless explicitly stated, plasmas consist of electrons and protons.

Low-β plasma	Size L (m)	n_e (m^{-3})	B (Tesla)	$E_{\rm max,obs}$ (eV)	$E_{\rm max,est}$ (eV)	Notes or assumptions
Laser Plasma (this work)	1×10^{-3}	1×10^{24}	50	$(4-7)\times10^{4}$	3×10^{4}	Cu^{+18} plasma
Magnetotail[5]	6×10^{8}	1×10^{5}	1×10^{-8}	3×10^{5}	4×10^{5}	*in-situ* measurement
Solar Flares[44,45]	1×10^{7}	1×10^{15}	2×10^{-2}	1×10^{8}	6×10^{10}	
X-ray Binary Disk Flares[46,47]	3×10^{4}	1×10^{24}	1×10^{4}	5×10^{8}	1×10^{14}	Cygnus X-3, $M=10M_\odot$, $R=R_S$
Crab Nebula Flares[7,8,23]	1×10^{17}	10^{6}	1×10^{-8}	5×10^{15}	2.4×10^{15}	pair plasma
Gamma Ray Bursts[48,49]	10^{4}	2×10^{35}	4×10^{9}	5×10^{9}	3×10^{20}	pair plasma
Magnetar Flares[50]	10^{4}	10^{41}	2×10^{11}	2×10^{8}	5×10^{20}	pair plasma, FRB 121102
AGN Disk Flares[46,51]	3×10^{11}	1×10^{17}	4	5×10^{8}	3×10^{17}	Seyfert 1 NGC 5548, $M=10^8M_\odot$, $R=R_S$
Radio Lobes[52]	3×10^{19}	0.1	5×10^{-10}	5×10^{11}	5×10^{16}	
Extragalactic Jets[53]	3×10^{19}	3×10^{1}	10^{-7}	7×10^{12}	1×10^{18}	3C 303

tor angle and $\theta-R$ pitch angle, a reconnection plane exists such that a particle accelerated from that plane would reach the detector.

Due to the particle injection scheme from $0<t<t_{\rm rise}$, the baseline spectrum is taken at $t=t_{\rm rise}$, in order to distinguish reconnection-accelerated electrons from injected electrons. The reconnection rate evolution shows that reconnection does not begin until $t>t_{\rm rise}$, further validating this approach. Figure 4d shows the formation of a non-thermal electron tail. The tail grows larger with time, up to a maximum (at $t\sim1.7t_{rise}$), and begins to decay back to a Maxwellian, as reconnection stops and accelerated particles escape the system through the open boundaries. The time of the maximally non-thermal spectrum corresponds well to the reconnection electric field time dependence, demonstrating push reconnection as the source of the accelerated particles.

Comparison of the experimental particle spectra with PIC simulations supports acceleration by the reconnection electric field as the primary acceleration mechanism that forms the non-thermal electron tail. This is evidenced by the angular dependence and accelerated energies of the non-thermal tails in experimental measurements. The strongest non-thermal components are seen in Channel 5, corresponding to its near-normal orientation. The strength of the bump decreases as the azimuthal angle grows more oblique. Acceleration by the out-of-plane reconnection electric field would be expected to produce this angular dependence: electrons with larger pitch angles would be directed into regions with high field, resulting in re-magnetization, preventing the electron from reaching the detector. This angular dependence of the accelerated electrons is confirmed by PIC simulations, as shown in Fig. 4e, where non-thermal electrons decrease with increasing pitch angle from the reconnection electric field direction.

Although the accelerated particle spectrum from simulations could not be obtained for the experimental value of $\omega_{pe}/\Omega_{ce}=6.33$ through scaling due to prohibitive computational cost (see Methods section), the simulation-determined scaling of the out-of-plane electric field is well-established. Using the extrapolated reconnection electric field value $E_\theta=2.18\ (1.64,2.92)\times10^7$ V/m, a simple estimate for the expected accelerated electron energy gain becomes $\Delta E\sim|q_e|E_\theta d$, where q_e is the electron charge, and d is a characteristic acceleration distance, here taken to be $d\sim1000$ μm. This predicts $16-29$ keV electrons, which is within a factor of 2 of the experimental bump of $\sim50-70$ keV.

Our inference of direct electric field acceleration operating in the experiments motivates estimating the corresponding attainable particle energies from this mechanism in representative low-β collisionless reconnecting plasmas throughout the Universe[43] and comparing to maximum inferred electron energies from observations. The result is shown in Table 1, where we have assumed that our experimental implications for the mostly electron-only reconnection regime can be extended to electron-ion or pair plasma reconnection regimes. This leads to the reconnection electric field $E_\theta=0.1V_AB$ typically found in collisionless reconnection[41]. Therefore, the upper bound for the energy of the accelerated electrons by the reconnection electric field is established by $E_{max,est}=eE_\theta d$, where d is a characteristic acceleration distance which is taken to the system size, L, for maximum energy.

The estimated maximum energy is within a factor of 2 for Earth's magnetotail and Crab nebula flares, implying that if this mechanism is responsible for acceleration of the most energetic electrons in these two cases, coherent acceleration over a distance comparable to the system size is required. In all other cases, the observed maximum electron energy is well below the estimated theoretical maximum energy, suggesting that if this mechanism is at work at all, it must operate over length scales much shorter than the system size but with properly distributed spread to populate the whole electron energy spectra. This is exactly the multi-scale nature illustrated by the reconnection phase diagram in large systems[2,43].

Nonetheless, our laser-powered capacitor coils offer a unique experimental reconnection platform in magnetically

driven low-β plasmas to further study acceleration of electrons (and ions) in various reconnection regimes[2,43] via direct detection of accelerated particles. The extent to which the same or different mechanisms of particle acceleration emerge in different regimes will be of great interest to determine in future laboratory research and may depend on the particular reconnection boundary conditions and system geometries. Although no other mechanisms are excluded, our results reported serve as the first direct confirmation of any hypothesized acceleration mechanism, by magnetic reconnection.

METHODS

Laser-powered capacitor coil target

Laser-powered capacitor coil targets are composed of parallel plates (the capacitor) connected by one or multiple wires (the coils). Holes are formed in the front (facing the driving laser) plate to allow the laser beam(s) to bypass the front plate and only hit the back plate. Superthermal hot electrons are generated during the intense laser-solid interaction, some of which manage to escape from the back plate. A strong current is therefore supplied to the U-shaped wires from back to front, due to the resultant potential difference between the plates.

We use capacitor coil targets made from 50 μm-thick copper. The capacitors are formed by two square parallel plates with length 1.5 mm, with an inter-plate distance of 600 μm. Two holes of radius 250 μm are formed in the front plate to accommodate OMEGA EP long-pulse beams 3 and 4. The plates are joined by one or two parallel U-shaped coils, with rectangular cross-section 50 μm $\times$ 100 μm. Each coil consists of two 500 μm straight sections, joined by a semicircular section with radius 300 μm. In two-coil targets, the coils are separated by 600 μm. Capacitor coil targets are fabricated by laser-cutting a design in 50 μm-thick sheet copper, then bending the coils into shape.

Particle spectra measurement using OU-ESM

The Osaka University - electron spectrometer is a time-integrated diagnostic that can provide angular resolution in either polar or azimuthal angles, relative to the target. This is accomplished by the use of 5 channels, each separated in angle by 5°. In the experiment, we chose the azimuthal angle spread, since this pitch angle allows for distinguishing between acceleration mechanisms in an axisymmetric setup, with symmetry in the polar direction.

After reaching the spectrometer, an electron first passes through a pinhole 700 μm wide and 2 cm deep. Separation of electron energies is accomplished with a set of permanent magnets placed along the detector line-of-sight, creating a magnetic field perpendicular to the line-of-sight. The $\vec{v} \times \vec{B}$ force deflects differently-energized electrons different distances along the detector length onto a BAS-TR image plate. In general, impacts closer to the detector entrance represent lower-energy electrons. In the experiment, magnets were chosen corresponding to electron energies in the 20 keV $-$ 1 MeV range.

The field of view and solid angle subtended by each channel are defined by the pinhole size $p = 700$ μm, distance to target $D = 37.5$ cm, and pinhole/collimator depth $d = 2$ cm. The field of view is given by FOV $= pD/d = 13.1$ mm, which is significantly larger than the target size and sufficient to capture electrons from the main interaction. The solid angle is $\Omega = P^2/D^2 = 3.5 \times 10^{-6}$ sr and provides the primary restriction for electrons reaching the detector.

The primary sources of error in interpreting OU-ESM data involve image plate response to energetic electrons and image plate scanning offsets. The image plate response is taken from Bonnet et al., 2013[54], and introduces a 28% uncertainty. In addition, image plate signals decay with time, so image plates are scanned at exactly 30 minutes after the shot for consistency in signal level. In interpreting the image plate, defining the edge of the magnets is critical to an accurate energy spectrum. Here, an uncertainty of approximately 5 pixels, or 0.5 mm is introduced, translating to an uncertainty in the spectrum energy.

Particle-in-cell simulation setup

The 2-D PIC simulation box has dimensions of $L_z = 4D_{\rm coil}$ and $L_R = 2D_{\rm coil}$ in the z and R directions, respectively, where $D_{\rm coil}$ is the inter-coil distance of $L = 600$ μm. To avoid the difficult boundary at $R = 0$, a minimum radius of $R_{\rm min} = 50$ μm was used. Two rectangular-cross-section coils of width $l_z = 100$ μm and height $l_R = 50$ μm are located at $R = 300$ μm and $z = \pm D_{\rm coil}/2 = \pm 300$ μm, matching experimental positions.

In the simulation, lengths are normalized to electron skin depth $d_e = c/\omega_{pe}$, and times are expressed in terms of the inverse electron plasma frequency ω_{pe}^{-1}. Due to the large Lundquist number, collisions are turned off in the simulation.

It is computationally untenable to perform a simulation with completely physical parameters, and so priorities must be made. An accurate particle spectrum is of great importance, so reducing ion-to-electron mass ratio m_i/m_e is undesirable. In addition, the plasma β has been shown to be a critical parameter in particle acceleration[55], so we maintain the physical β in the simulation. To reduce computational time, we instead use artificially small values of the electron plasma frequency to electron gyrofrequency ω_{pe}/Ω_{ce}. By keeping β constant, a reduced ω_{pe}/Ω_{ce} represents an artificially strong magnetic field, coupled to an artificially hot plasma. Scaling relations for electromagnetic field strength can be established as a function of ω_{pe}/Ω_{ce} in order to extrapolate to physical conditions. The physical $\omega_{pe}/\Omega_{ce} = 6.33$, and simulations are run for reduced values $\omega_{pe}/\Omega_{ce} = 6.33/3$, $6.33/4$, $6.33/6$, $6.33/12$, $6.33/16$, and $6.33/24$.

Cell size is limited by the Debye length, so the number of cells changes with ω_{pe}/Ω_{ce}. At $\omega_{pe}/\Omega_{ce} = 6.33/4$, the number of cells is $n_z \times n_R = 1440 \times 720$, spanning $L_z \times L_R = 451.6d_e \times 225.8d_e$. 200 macro-particles of each species are

initialized per cell. The achievable cell size and number of macro-particles per cell also limit a viable scaling of accelerated electron spectra to be established for the small electron diffusion region where electrons are demagnetized, and thus are free to be accelerated by the reconnection electric field.

For physical $\omega_{pe}/\Omega_{ce} = 6.33$, the simulation is initialized with a uniform Maxwellian plasma with $n_e = 10^{18}$ cm^{-3}, $n_i = n_e/Z = 5.6 \times 10^{16}$ cm^{-3}, $T_e = T_i = 400$ eV to match experimental parameters. Compared to experiment, a lower initial plasma density is used due to the inclusion of a particle injection scheme from the coil region. A representative magnetic field strength $B_0 = 50.7$ T is taken to be the upstream magnetic field at $z = -D_{\rm coil}/4$ from the center between the coils. The simulation β is therefore 0.063. Due to the artificially reduced ω_{pe}/Ω_{ce} values, ion and electron temperatures and coil magnetic fields are artificially increased, while keeping density constant to maintain plasma β.

Electrically conducting boundary conditions are set for fields, and open boundary conditions[56] are set for particles in the z and R directions (periodic boundary conditions are set for θ). The open boundary conditions prevent accelerated particles that would otherwise escape the system from being re-accelerated. Our choice therefore prevents an over-estimation of particle acceleration that would be inevitable with periodic or reflecting boundaries.

At $t = 0$, electromagnetic fields are set to 0. The capacitor coil currents are modeled by injecting currents with the following time profile:

$$I_{\rm coil}(t) = \begin{cases} I_0(t/t_{\rm rise}), & t < t_{\rm rise} \\ I_0 \exp(-(t-t_{\rm rise})/t_{\rm decay}), & t \geq t_{\rm rise} \end{cases} \quad (1)$$

where $t_{\rm rise} = 1$ ns, $t_{\rm decay} = 8.6$ ns, and $I_0 = 57$ kA match experimental measurements. Currents are oriented into the page ($-\theta$ direction). The coil magnetic fields are then calculated from the current distribution within the coils.

The reconnection plasma primarily emanates from the coils, due to ablation of copper plasma by Ohmic heating within the coils and irradiation by x-rays from the laser interaction. In contrast, the plasma generated at the laser spot takes a few nanoseconds to flow into the reconnection region, and does not play a significant role in reconnection, particularly during the push phase. To simulate the coil plasma, we use a particle injection scheme: a volume injector is implemented around the coils, with a Gaussian spatial profile (Gaussian width and height are set to l_z and l_R, respectively), and a linear time-dependence from $t = 0 - 1$ ns. The injection rate is tuned to match experimental density measurements. Without the particle injection scheme, density voids form around the coils, as the strong magnetic field pressure pushes out plasma as the magnetic field diffuses outwards from the coils.

REFERENCES

[1] M. Yamada, R. Kulsrud, and H. Ji, Rev. Mod. Phys. **82**, 603 (2010).

[2] H. Ji, W. Daughton, J. Jara-Almonte, A. Le, A. Stanier, and J. Yoo, "Magnetic reconnection in the era of exascale computing and multiscale experiments," submitted to Nat. Rev. Phys. (2021).

[3] R. Blandford, Y. Yuan, M. Hoshino, and L. Sironi, Space Science Rev. **207**, 291 (2017).

[4] S. Masuda, T. Kosugi, H. Hara, S. Tsuneta, and Y. Ogawara, Nature **371**, 495 (1994).

[5] M. Øieroset, R. P. Lin, T. D. Phan, D. E. Larson, and S. D. Bale, Phys. Rev. Lett. **89**, 195001 (2002).

[6] S. Krucker, H. S. Hudson, L. Glesener, S. M. White, S. Masuda, J.-P. Wuelser, and R. P. Lin, Astrophys. J. **714**, 1108 (2010).

[7] A. Abdo, M. Ackermann, M. Ajello, A. Allafort, L. Baldini, J. Ballet, G. Barbiellini, D. Bastieri, K. Bechtol, and R. Bellazzini, Science **331**, 739 (2011).

[8] M. Tavani, A. Bulgarelli, V. Vittorini, A. Pellizzoni, E. Striani, P. Caraveo, M. Weisskopf, A. Tennant, G. Pucella, and A. Trois, Science **331**, 736 (2011).

[9] B. Chen, C. Shen, D. E. Gary, K. K. Reeves, G. D. Fleishman, S. Yu, F. Guo, S. Krucker, J. Lin, G. M. Nita, and X. Kong, Nature Astronomy **4**, 1140 (2020).

[10] G. Drenkhahn and H. C. Spruit, Astro. Astrophys. **391**, 1141 (2002).

[11] L. Sironi and A. Spitkovsky, Astrophys. J. Lett. **783**, L21 (2014).

[12] G. R. Werner, D. A. Uzdensky, B. Cerutti, K. Nalewajko, and M. C. Begelman, Astrophys. J. Lett. **816**, L8 (2016).

[13] X. Li, F. Guo, H. Li, and G. Li, Astrophys. J. **843**, 21 (2017).

[14] F. Guo, Y.-H. Liu, X. Li, H. Li, W. Daughton, and P. Kilian, Phys. Plasmas **27**, 080501 (2020).

[15] J. T. Dahlin, Phys. Plasmas **27**, 100601 (2020).

[16] J. F. Drake, M. Swisdak, H. Che, and M. A. Shay, Nature **443**, 553 (2006).

[17] M. Hoshino, T. Mukai, T. Terasawa, and I. Shinohara, J. Geophys. Res. **106**, 25979 (2001).

[18] J. Egedal, A. Le, and W. Daughton, Phys. Plasmas **20**, 061201 (2013).

[19] S. Zenitani and M. Hoshino, Astrophys. J. Lett. **562**, L63 (2001).

[20] L. Gao, H. Ji, G. Fiksel, W. Fox, M. Evans, and N. Alfonso, Physics of Plasmas **23**, 043106 (2016).

[21] A. Chien, L. Gao, H. Ji, Y. Xiaoxia, E. Blackman, H. Chen, P. Efthimion, G. Fiksel, D. Froula, K. Hill, K. Huang, Q. Lu, J. Moody, and P. Nilson, Physics of Plasmas **26**, 062113 (2019).

[22] A. Chien, L. Gao, S. Zhang, H. Ji, E. Blackman, H. Chen, G. Fiksel, K. Hill, and P. Nilson, Phys. Plasmas **28**, 052105 (2021).

[23] J. J. Kroon, P. A. Becker, J. D. Finke, and C. D. Dermer, Astrophys. J. **833**, 157 (2016).

[24] J. T. Dahlin, J. F. Drake, and M. Swisdak, Physics of Plasmas **21**, 092304 (2014), https://doi.org/10.1063/1.4894484.

[25] J. T. Dahlin, J. F. Drake, and M. Swisdak, Physics of Plasmas **23**, 120704 (2016), https://doi.org/10.1063/1.4972082.

[26] S. R. Totorica, T. Abel, and F. Fiuza, Phys. Rev. Lett. **116**, 095003 (2016).

[27]P. V. Savrukhin, Physical Review Letters **86**, 3036 (2001).
[28]I. Klimanov, A. Fasoli, T. P. Goodman, and the TCV team, Plasma Physics and Controlled Fusion **49**, L1 (2007).
[29]A. M. DuBois, A. F. Almagri, J. K. Anderson, D. J. Den Hartog, J. D. Lee, and J. S. Sarff, Phys. Rev. Lett. **118**, 075001 (2017).
[30]P. M. Nilson, L. Willingale, M. C. Kaluza, C. Kamperidis, S. Minardi, M. S. Wei, P. Fernandes, M. Notley, S. Bandyopadhyay, M. Sherlock, R. J. Kingham, M. Tatarakis, Z. Najmudin, W. Rozmus, R. G. Evans, M. G. Haines, A. E. Dangor, and K. Krushelnick, Phys. Rev. Lett. **97**, 255001 (2006).
[31]L. Willingale, P. M. Nilson, M. C. Kaluza, A. E. Dangor, R. G. Evans, P. Fernandes, M. G. Haines, C. Kamperidis, R. J. Kingham, C. P. Ridgers, M. Sherlock, A. G. R. Thomas, M. S. Wei, Z. Najmudin, K. Krushelnick, S. Bandyopadhyay, M. Notley, S. Minardi, M. Tatarakis, and W. Rozmus, Phys. Plasmas **17**, 043104 (2010).
[32]J. Zhong, Y. Li, X. Wang, J. Wang, Q. Dong, C. Xiao, S. Wang, X. Liu, L. Zhang, L. An, F. Wang, J. Zhu, Y. Gu, X. He, G. Zhao, and J. Zhang, Nature Phys. **6**, 984 (2010).
[33]G. Fiksel, W. Fox, A. Bhattacharjee, D. H. Barnak, P. Y. Chang, K. Germaschewski, S. X. Hu, and P. M. Nilson, Phys. Rev. Lett. **113**, 105003 (2014).
[34]A. E Raymond, C. Dong, A. Mckelvey, C. Zulick, N. Alexander, A. Bhattacharjee, P. T Campbell, H. Chen, V. Chvykov, E. Del Rio, P. Fitzsimmons, W. Fox, B. Hou, A. Maksimchuk, C. Mileham, J. Nees, P. M Nilson, C. Stoeckl, A. Thomas, and L. Willingale, Physical Review E **98**, 043207 (2018).
[35]S. C. Wilks, A. B. Langdon, T. E. Cowan, M. Roth, M. Singh, S. Hatchett, M. H. Key, D. Pennington, A. MacKinnon, and R. A. Snavely, Physics of Plasmas **8**, 542 (2001).
[36]M. Yamada, H. Ji, S. Hsu, T. Carter, R. Kulsrud, N. Bretz, F. Jobes, Y. Ono, and F. Perkins, Physics of Plasmas **4**, 1936 (1997).
[37]T. D. Phan, J. P. Eastwood, M. A. Shay, J. F. Drake, B. U. Ö. Sonnerup, M. Fujimoto, P. A. Cassak, M. Øieroset, J. L. Burch, R. B. Torbert, A. C. Rager, J. C. Dorelli, D. J. Gershman, C. Pollock, P. S. Pyakurel, C. C. Haggerty, Y. Khotyaintsev, B. Lavraud, Y. Saito, M. Oka, R. E. Ergun, A. Retino, O. Le Contel, M. R. Argall, B. L. Giles, T. E. Moore, F. D. Wilder, R. J. Strangeway, C. T. Russell, P. A. Lindqvist, and W. Magnes, Nature **557**, 202 (2018).
[38]K. J. Bowers, B. J. Albright, L. Yin, B. Bergen, and T. J. T. Kwan, Phys. Plasmas **15**, 055703 (2008).
[39]D. Uzdensky and R. Kulsrud, Phys. Plasmas **13**, 062305 (2006).
[40]J. Birn, J. Drake, M. Shay, B. Rogers, R. Denton, M. Hesse, M. Kuznetsova, Z. Ma, A. Bhattachargee, A. Otto, and P. Pritchett, J. Geophys. Res. **106**, 3715 (2001).
[41]P. Cassak, Y.-H. Liu, and M. Shay, J. Plasma Phys. **83**, 715830501 (2017).
[42]P. Sharma Pyakurel, M. A. Shay, T. D. Phan, W. H. Matthaeus, J. F. Drake, J. M. TenBarge, C. C. Haggerty, K. G. Klein, P. A. Cassak, T. N. Parashar, M. Swisdak, and A. Chasapis, Physics of Plasmas **26**, 082307 (2019), https://doi.org/10.1063/1.5090403.
[43]H. Ji and W. Daughton, Phys. Plasmas **18**, 111207 (2011).
[44]N. Vilmer, Philosophical Transactions of the Royal Society of London Series A **370**, 3241 (2012).
[45]J. C. Raymond, S. Krucker, R. P. Lin, and V. Petrosian, Space Science Rev. **173**, 197 (2012).
[46]J. Goodman and D. Uzdensky, Astrophys. J. **688**, 555 (2008).
[47]F. Cangemi, J. Rodriguez, V. Grinberg, R. Belmont, P. Laurent, and J. Wilms, Astro. Astrophys. **645**, A60 (2021).
[48]R. Sari and T. Piran, Astrophys. J. **520**, 641 (1999).
[49]D. Uzdensky, "Magnetic reconnection in extreme astrophysical environments," (2011), published in Space Sci. Rev., DOI: 10.1007/s11214-011-9744-5.
[50]A. M. Beloborodov, Astrophys. J. **843**, L26 (2017).
[51]G. Torricelli-Ciamponi, P. Pietrini, and A. Orr, Astro. Astrophys. **438**, 55 (2005).
[52]F. Massaro and M. Ajello, Astrophys. J. Lett. **729**, L12 (2011).
[53]J. Kataoka, P. Edwards, M. Georganopoulos, F. Takahara, and S. Wagner, Astro. Astrophys. **399**, 91 (2003).
[54]T. Bonnet, M. Comet, D. Denis-Petit, F. Gobet, F. Hannachi, M. Tarisien, M. Versteegen, and M. M. Aléonard, Review of Scientific Instruments **84**, 103510 (2013), https://doi.org/10.1063/1.4826084.
[55]D. Ball, L. Sironi, and F. Özel, Astrophys. J. **862**, 80 (2018).
[56]W. Daughton, J. Scudder, and H. Karimabadi, Physics of Plasmas **13**, 072101 (2006), https://doi.org/10.1063/1.2218817.